Plasma beta dependence of ion temperature gradient driven turbulence influenced by Shafranov shift

M. Niiro, A. Ishizawa, Y. Nakamura, S. Maeyama[1], and T.-H. Watanabe[1]

Graduate School of Energy Science,

Kyoto University, Uji, Kyoto 611-0011, Japan and

[1]*Department of Physics, Nagoya University, Nagoya, 464-8602, Japan*

(Dated: March 26, 2023)

Abstract

Plasma β dependence of ion temperature gradient (ITG) driven turbulence is investigated using gyrokinetic simulations, where β is the normalized pressure. In our β scan, self-consistent magnetohydrodynamic (MHD) equilibrium state is numerically calculated for each value of β. It is found that the influence of the Shafranov shift cancels out the electromagnetic stabilizing effect on the ITG mode, and the growth rate of the ITG mode is accordingly unchanged as β increases. As a result, the turbulent energy transport does not decrease with β as suggested by the s-α model [Ishizawa et al 2019 Phys. Rev. Lett. 123 025003]. A significant difference from the s-α model is the increase of the energy transport with β. It is also found that the critical onset β value for the kinetic ballooning mode (KBM) is significantly increased by the influence of the Shafranov shift. The cancellation of the electromagnetic stabilization by the Shafranov shift is explained by the decrease of magnetic drift frequency in the dispersion relation of electromagnetic ITG modes obtained by using a fluid approximation.

I.   INTRODUCTION

Drift-wave turbulence is the main cause of heat and particle transport in tokamak plasmas [1, 2]. Understanding of the β dependence of turbulent transport is important for predicting the generation of bootstrap current which is needed for steady operation of tokamaks and the fusion reaction rate which is directly related to the plasma pressure, and thus the β dependence of the confinement is extensively studied in experiments [3–7], where β is the plasma pressure normalized by the magnetic energy. In finite β plasmas, turbulent fluctuations are electromagnetic because β appears in gyrokinetic Ampere's law, and thus electromagnetic drift-waves such as the kinetic ballooning mode (KBM) can be unstable [8–10]. The electromagnetic drift-wave turbulence is studied by gyrokinetic analysis [11], and magnetic fluctuations are known to cause a stabilizing effect on the ion temperature gradient (ITG) mode [12], suggesting a reduction of turbulent transport with increasing β [13–17]. The electromagnetic stabilizing effect on the ITG mode is demonstrated in the analysis of tokamaks including JET and ASDEX Upgrade [18–23] and stellarators [24, 25].

Recently, it is found that the turbulent transport due to the ITG mode does not decrease with increasing β [26]. This is because the electromagnetic stabilizing effect on the linear growth rate of the ITG mode is weakened by the influence of the Shafranov shift, and in addition, the zonal flow suppression by the magnetic perturbations is enhanced with increasing β through the Maxwell stress, which is related to the reduction of the zonal flow amplitude by the magnetic stochasticity [27–29]. The analysis for several tokamaks including JET and ASDEX Upgrade shows that, when the magnetic shear is small $s \ll 1$, the influence of the Shafranov shift is weakened [26], and accordingly the electromagnetic stabilization of the ITG mode is prominent with increasing β. This explains the electromagnetic stabilization of turbulence observed in the core region of high-β JET hybrid discharge with small magnetic shear [18, 19, 21–23, 30, 31], which exhibits the heat flux reduction with increasing β. The minimal and widely used model including the change of background magnetic field due to finite β is the $s - \alpha$ model [12, 32–35], and its effect on the β dependence of turbulent transport is significant [26], however, it is better to use self-consistent MHD equilibrium states calculated by some numerical code for predicting the β dependence of turbulent transport precisely.

In this paper, we investigate the β dependence of drift-wave instabilities and associated

turbulent transport using the GKV code [36–38]. In our analysis, the MHD equilibrium of tokamak plasma is calculated by the VMEC code for each value of β [39]. The numerical equilibrium states are consistent with the Cyclone base case parameter, and accurately include not only the Shafranov shift but also other changes of magnetic field structure due to a finite β value. It is found that the linear growth rate of the ITG mode is almost unchanged as β increases when the background magnetic field change is included, while the linear growth rate decreases with β when we fix the background magnetic field with increasing β, implying that the electromagnetic stabilization is canceled out by the influence of the change of background magnetic field including the Shafranov shift. As a result, the magnetic field change enhances the turbulent transport, and the ion and electron energy diffusion coefficients increase with increasing β. The mechanism of the cancellation is turned out to be the decrease of magnetic drift frequency by the Shafranov shift by using the linear dispersion relation of electromagnetic ITG modes derived by a fluid approximation.

The organization of the remainder of this paper is as follows. Section II describes our numerical model and parameter setting. Section III presents results from linear analysis. Section IV presents nonlinear simulation results. We conclude with a summary of our results in Sec. V.

II. SIMULATION MODEL

We consider the Cyclone base case DIII-D plasma which has a circular cross-section [13], and calculate the MHD equilibrium state of this plasma using the VMEC code [39]. We use a pressure profile which is consistent with the CBC parameter at $\rho = 0.5$ and has a peak of pressure gradient $dp/d\rho$ at $\rho \simeq 0.5$. The pressure profile and safety factor are shown in Fig. 1. The pressure gradient length at $\rho = 0.5$ is

$$-\frac{R_0}{a}\frac{1}{p}\frac{dp}{d\rho}(\rho = 0.5) = \frac{R_0}{L_n} + \frac{1}{1 + T_e/T_i}\frac{R_0}{L_{Ti}} + \frac{T_e/T_i}{1 + T_e/T_i}\frac{R_0}{L_{Te}} = 9.1.$$

where R_0 is the major radius of the center of the last closed flux surface and a is the minor radius of the last closed flux surface. The values of the profiles at $\rho = 0.5 \equiv \rho_0$ are set to the CBC parameter: $q_0 = 1.4$, $\hat{s} = 0.78$, $T_i = T_e$, and $\rho_0 a/R_0 = 0.18$.

The equilibrium magnetic field configuration obtained from the VMEC code exhibits the Shafranov shift as shown in Fig. 2. The Shafranov shift monotonically increases with β as

shown in Fig. 3. The influence of the magnetic field change (MFC) due to the increase of β is shown in the profiles of magnetic field strength B along a magnetic field line in Fig. 4 (a), the square of the perpendicular wavenumber $k_\perp^2$ in Fig. 4 (b), and the ion magnetic drift frequency ω_{di} in Fig. 4 (c) as well as the corresponding profiles from the $s - \alpha$ model. It is remarked that the pressure gradient in the curvature drift velocity, which is discussed in Ref. [40], is neglected in this work. It is expected that the pressure gradient in the curvature drift velocity and the compression magnetic field perturbation $\tilde{B}_\parallel$ do not influence the ITG modes in low-β regime, while they can influence the critical onset β value of the KBM. Reference [40] presented that the critical onset β of KBM is significantly changed when one of the pressure gradient in the curvature drift velocity and $\tilde{B}_\parallel$ is included, however, when both of them are included, then their influence on the growth rate is small and leads to a little higher critical onset β of KBM. Thus, we expect that neglecting both of them in our analysis does not cause significant impact on our simulation results. The profile of magnetic field strength is slightly changed by the MFC in Fig. 4 (a). On the other hand, the perpendicular wavenumber $k_\perp^2$ is reduced around $z = 0$ by the MFC. In addition, the $k_\perp^2$ by the MFC is smaller than that from the $s - \alpha$ model. These are because the large aspect ratio is assumed in the $s - \alpha$ model. We have confirmed that a large-aspect-ratio equilibrium calculated by the VMEC code exhibits similar $k_\perp^2$ and ω_{di} profiles to those from the $s - \alpha$ model, however, the magnetic field strength is significantly different from that in Fig. 4 (a) as shown in Appendix, and thus we do not use the large-aspect-ratio equilibrium in our analysis. The MFC also influences the magnetic drift frequency ω_{di}. The absolute value of ω_{di} for the MFC at $z \simeq 0$ becomes small as β increases, and the finite β effect is more prominent at $z \simeq \pm\pi/2$ due to the local magnetic shear. In addition, the absolute value of ω_{di} is smaller than that from the $s - \alpha$ model.

In our gyrokinetic analysis, we use the GKV code [36–38]. The major radius of the shifted magnetic axis R_{ax} is used to normalize global lengths such as density and temperature gradient lengths, so that $R_{\mathrm{ax}}/L_n = 2.23$ and $R_{\mathrm{ax}}/L_T = 6.90$ at $\beta = 0$, while $R_{\mathrm{ax}}/L_n = 2.31$ and $R_{\mathrm{ax}}/L_T = 7.15$ at $\beta = 2.4\%$, where $L_T \equiv L_{Ti} = L_{Te}$. In our linear analysis, grid points of 640, 128, and 16 in the z, $v_\parallel$, and μ directions are distributed in $-10\pi \leq z \leq 10\pi$, $-4v_{Ts} \leq v_\parallel \leq 4v_{Ts}$, and $0 \leq \mu B_0/T_s \leq 8$, respectively. The collision frequencies are set to $\nu_i = \nu_e = 0$. In our nonlinear simulations, grid points of 128, 128, and 16 are assigned to $-\pi \leq z \leq \pi$, $-4v_{Ts} \leq v_\parallel \leq 4v_{Ts}$, and $0 \leq \mu B_0/T_s \leq 4$ in the z, $v_\parallel$, and μ directions,

respectively. The wavenumbers in the Fourier space are represented by $k_x = k_{x,min}m$ and $k_y = k_{y,min}n$, where $0 \leq m \leq 96$, $-24 \leq n \leq 24$ and $(k_{x,min}\rho_{Ti}, k_{y,min}\rho_{Ti}) = (0.06, 0.05)$. The collision frequencies are set to $\nu_i = \nu_e = 10^{-5}\ [v_{Ti}/R_0]$.

III. LINEAR ANALYSIS

In this section, we present the β dependence of drift-wave instabilities in the CBC tokamak plasma. In the magnetic field change (MFC) scan, the MHD equilibrium is calculated for each value of β using the VMEC code, while in the magnetic field fixed (MFF) scan the MHD equilibrium remains unchanged and is fixed to the one for a β value such as $\beta = 0$.

Figure 5 shows the linear growth rate γ and real frequency ω as a function of the poloidal wavenumber k_y at $\beta = 0.4\%$ and 2.4%. The ITG mode dominates at low wavenumber and the trapped electron mode (TEM) at high wavenumber for both of the MFC and MFF. For the MFF, the linear growth rate of the ITG mode at $\beta = 2.4\%$ is a half of that at $\beta = 0.4\%$ because of the electromagnetic stabilizing effect due to the increase of magnetic fluctuations with increasing β. For the MFC, by contrast, the growth rate at $\beta = 2.4\%$ is similar to that at $\beta = 0.4\%$, and the reduction of the growth rate is very small compared to the MFF. Thus, the electromagnetic stabilization is almost canceled out by the MFC, i.e. the Shafranov shift due to finite β. It is remarked that there is no significant change in the TEM by the increase of β.

Figure 6 (a) shows the linear growth rate as a function of β for $k_y\rho_{Ti} = 0.2$. The linear growth rate of the ITG mode remains almost unchanged as β increases for the MFC scan (red curve), while the growth rate decreases with β for the MFF scan using the equilibrium at $\beta = 0$ (blue curve), and thus the Shafranov shift cancels out the electromagnetic stabilization. In addition, the Shafranov shift significantly increases the critical onset β value for the KBM. The KBM is destabilized at $\beta = 2.8\%$ for the MFF scan, while the growth rate of the ITG mode remains unchanged up to $\beta = 4.8\%$ for the MFC scan, and thus the critical onset β value for the KBM is significantly raised by the MFC. It is remarked that the critical β for the KBM in the MFF without Shafranov shift is similar to $\beta = 2\beta_i \simeq 2.6\%$ from the $s - \alpha$ model in Fig. 1 of Ref. [26] which exhibits no difference in the KBM threshold between the MFC and MFF, where $\beta_i = \beta/(1 + T_e/T_i)$. Hence, the KBM threshold is significantly increased when we take into account the influence of the Shafranov shift by

means of numerical MHD equilibrium states. It is remarked that in our analysis the pressure gradient in the curvature drift velocity and the compressional magnetic field perturbation $\tilde{B}_\parallel$ are neglected. Our conclusion on the ITG modes is not influenced by them because the ITG modes are unstable at low-β regime. On the other hand, the critical onset β value of the KBM can be influenced by these effects because of high β. However, when we include both the pressure gradient in the curvature drift velocity and $\tilde{B}_\parallel$ simultaneously, then the results are not so different from those obtained by neglecting both of them as presented in Ref. [40]. The electromagnetic stabilization is also significant for the MFF at $k_y\rho_{Ti} = 0.4$ and 0.6 as indicated by blue curves in Figs. 6 (b) and (c). On the other hand, the MFC scans for $k_y\rho_{Ti} = 0.4$ and 0.6 (red curves) show that the linear growth rate of the ITG mode almost remains unchanged as β increases. Thus, the electromagnetic stabilization is canceled out by the influence of the Shafranov shift.

So far, the MFF β scan is carried out by using the equilibrium at $\beta = 0$, i.e. without the Shafranov shift. Here, the MFF scans are carried out by using the equilibrium states at $\beta = 1.2\%$ and 2.4% in Fig. 6, but the equilibrium is fixed during the scan, i.e. the amplitude of the Shafranov shift is fixed. When we use the equilibrium at $\beta = 1.2\%$ for the MFF scan, the Shafranov shift is finite but unchanged with β, then the linear growth rate decreases as β increases for $k_y\rho_{Ti} = 0.2$, 0.4 and 0.6 as indicated by green curves, suggesting the electromagnetic stabilization. The electromagnetic stabilization is observed even when we use the equilibrium at $\beta = 2.4\%$ for the MFF scan as shown by black curves in Figs. 6 (a), (b) and (c). Comparing the MFF using the equilibrium at $\beta = 0$ and the MFF using the equilibrium at $\beta = 2.4\%$ for $k_y\rho_{Ti} = 0.4$ in Fig. 6 (b), their difference at $\beta = 2.4\%$ is much larger than that at $\beta = 0$. This suggests that the increase of the growth rate for the MFC from that for the MFF using the equilibrium at $\beta = 0$ is mainly caused by magnetic fluctuations, because the amplitude of magnetic fluctuations is larger at $\beta = 2.4\%$ than that at $\beta = 0$. It is noted that, in the analysis of JET [19] and ASDEX Upgrade [20], the MFF β scan is carried out using the equilibrium states at a finite β.

Here, we discuss the destabilizing mechanism of the ITG mode by the MFC based on the change in $k_\perp^2$ and ω_{di}. It is commonly understood that a larger perpendicular wavenumber $k_\perp$ has a stabilizing effect on ballooning type instabilities, while the magnetic drift frequency ω_{di} causes instabilities at the bad curvature region when $\omega_{di}\omega_{*pi} > 0$. We have observed that the perpendicular wavenumber $k_\perp^2$ is reduced around $z = 0$ by the MFC, and the absolute

6

value of the magnetic drift frequency ω_{di} becomes small at $z \simeq 0$ as β increases in Fig. 4. These suggest that the impact of the Shafranov shift on $k_\perp^2$ (ω_{di}) enhances (reduces) the growth rate of instabilities. However, the influence of the MFC on the electromagnetic stabilization of the ITG mode through $k_\perp^2$ and ω_{di} is turned out to be otherwise as shown in Fig. 7. Figure 7 shows that the growth rate of the ITG mode for the changed magnetic field only in ω_{di} case ($\omega_{di}C$) and for the changed magnetic field only in $k_\perp^2$ case ($k_\perp^2 C$) in comparison with the MFC and MFF for $k_y \rho_{Ti} = 0.2$, 0.4, and 0.6. The growth rate for the $\omega_{di}C$ is higher than that of the MFF and is close to the MFC. On the other hand, the growth rate for the $k_\perp^2 C$ is a little higher or lower than that of the MFF depending on β. Thus, the enhancement of the growth rate by the magnetic field change in ω_{di} is the dominant cause of the cancellation of the electromagnetic stabilization.

The destabilization of the ITG mode by the MFC through ω_{di} can be understood by revisiting an analytical study on electromagnetic ITG modes [12]. The linear dispersion relation for the electromagnetic ITG mode is obtained by assuming (1) the local limit $\nabla_\parallel \to ik_\parallel$, $\omega_{ds}(z) \to \omega_{ds}(z = 0)$, and $\omega_{*s}(z) \to \omega_{*s}(z = 0)$, (2) the fast electron streaming along the field line $\omega \approx \omega_{de} \ll k_\parallel v_{Te}$, and (3) the fluid approximation $\omega_{Di} \ll \omega$, $k_\parallel v_\parallel \ll \omega$, $k_\perp \rho_{Ti} \ll 1$, where s denotes the particle species. Then, we obtain the following dispersion relation [12]

$$1 - \frac{\omega_{*e}}{\omega} - \frac{k_\parallel^2 c_s^2}{\omega^2}\left(1 - \frac{\omega_{*pi}}{\omega}\right) + \frac{T_e}{T_i}\left(k_\perp^2 \rho_{Ti}^2 - \frac{\omega_{Di}}{\omega}\right)\left(1 - \frac{\omega_{*pi}}{\omega}\right)F = 0, \tag{1}$$

where

$$F = 1 - \frac{T_i}{T_e}\frac{\omega(\omega - \omega_{*e}) - k_\parallel^2 c_s^2(1 - \omega_{*pi}/\omega)}{2k_\perp^2 \rho_{Ti}^2 k_\parallel^2 v_{Ti}^2/\beta_i - \omega_{Di}(\omega - \omega_{*pe})} \tag{2}$$

is the electromagnetic stabilizing factor, $\omega_{Di} = -(2cT_i k_y)/(eB_0 R_0)$, $\omega_{*s} = -(cT_s k_y)/(q_s B_0 L_n)$, $\omega_{*ps} = \omega_{*s}(1 + \eta_s)$, $c_s^2 = v_{Ti}^2 T_e/T_i$, $v_{Ti}^2 = T_i/m_i$, $\eta_s = d\ln T_s/d\ln n_0$, $q_i = e$, and $q_e = -e$, $\beta_i = \beta/(1 + T_e/T_i)$ is the ion normalized pressure. It is remarked that $\beta_i = \beta/2$ in our numerical simulations. The first three terms represent the propagation of the drift wave and the drive of the slab ITG mode. The last term represents the drive of the toroidal ITG mode at the outer-board of the torus, i.e. the ITG mode is unstable for $\omega_{Di}\omega_{*pi} > 0$. It is remarked that the coefficient of this term T_e/T_i implies that the ITG mode is more unstable for a larger T_e/T_i. Equation (1) reduces to the dispersion relation for the pure slab ITG mode in the limit $\omega_{Di} \to 0$, while the pure toroidal ITG mode in the limit $k_\parallel^2 c_s^2/\omega^2 \to 0$. The factor F of the destabilizing force term represents the electromagnetic stabilizing effect on the ITG mode, and the electromagnetic stabilization vanishes, i.e.

$F \to 1$, in the electrostatic limit $\beta_i \to 0$ ($v_A = v_{Ti}/\sqrt{\beta_i} \to \infty$). For small β_i and using $\omega_{\text{ITG}} \approx \omega_{Di} \ll \omega_{*pi}$ for the toroidal ITG mode, the stabilizing factor F is reduced to

$$F = 1 - \beta_i \frac{\omega_{Di}\omega_{*i} + k_\parallel^2 v_{Ti}^2 \omega_{*pi}/\omega_{Di}}{2k_\perp^2 \rho_{Ti}^2 k_\parallel^2 v_{Ti}^2} + O(\beta_i^2). \tag{3}$$

This implies that the electromagnetic stabilization is enhanced by reducing $k_\perp^2$, while the stabilizing effect is suppressed by reducing ω_{Di}. It is remarked that $k_\parallel^2 v_{Ti}^2 \omega_{*pi}$ is the driving force of the slab ITG mode, and thus this term is small for the toroidal ITG mode. At finite β_i, the sign of F (Eq. (2)) is flipped from positive to negative at a critical β_i, so that the electromagnetic effect is changed from stabilizing to destabilizing. By using $\omega_{\text{ITG}} \approx \omega_{Di} \ll \omega_{*pi}$ for the toroidal ITG mode, $F = 0$ in Eq. (2) gives the critical β [12]

$$\beta_{it} = \frac{2k_\perp^2 \rho_{Ti}^2 k_\parallel^2 v_{Ti}^2}{\omega_{Di}(\omega_{*i} - \omega_{*pe}) + k_\parallel^2 v_{Ti}^2 \omega_{*pi}/\omega_{Di}}. \tag{4}$$

This formula implies that the electromagnetic stabilization is enhanced by reducing $k_\perp^2$, whereas the stabilizing effect is suppressed by reducing ω_{Di}. Combining the results at small β_i by Eq. (3) and finite β_i by Eq. (4), the β dependence of the growth rate can be schematically drawn in Fig. 8. Thus, the influence of magnetic fluctuations on the suppression of the ITG mode through $k_\perp^2$ and ω_d is opposite to the conventional consideration about the influence of $k_\perp^2$ and ω_d on ballooning instabilities as shown from the $s - \alpha$ model [26], though the influence of $k_\perp^2$ is very small in Ref. [26].

The above discussion is helpful for understanding the influence of the Shafranov shift on the ITG mode through $k_\perp^2$ and ω_{di} shown in Fig. 7. Figure 8 suggests that the linear growth rate is increased by smaller ω_{di} due to the magnetic field change (MFC), because the MFC reduces the amplitude of ω_{di} as shown in Fig. 4 (c). On the other hand, the linear growth rate is decreased by smaller $k_\perp$ due to the MFC, because the MFC reduces $k_\perp^2$ as shown in Fig. 4 (b), although the decrease of γ is subtle in Fig. 7 as suggested in Ref. [26]. As a result, the Shafranov shift enhances the ITG mode through ω_{di} as shown in Fig. 7. In our simulations, the enhancing effect of reduced ω_{di} on the ITG mode overcomes the suppression effect of reduced $k_\perp^2$, and thus the influence of Shafranov shift on ω_{di} is the dominant cause for the cancellation of electromagnetic stabilization of the ITG mode.

In addition, the electromagnetic stabilization is enhanced by reducing $k_\parallel^2$ as shown by Eqs. (3) and (4). This implies that the weak magnetic shear is very effective for realizing

electromagnetic stabilization [26], because the mode structure extends along the magnetic field line, i.e. $k_\parallel$ is small when the magnetic shear is small.

IV. NONLINEAR SIMULATIONS

In this section, the turbulent transport is evaluated by nonlinear simulations. Figure 9 shows the β dependence of the energy transport coefficients χ_i and χ_e normalized by the gyro-Bohm unit for the MFC and MFF, where $\chi_s = Q_s L_{Ts}$, $Q_s = Q_{es,s} + Q_{em,s}$,

$$Q_{es,s} = \sum_{\mathbf{k}_\perp} \left\langle Re \left[\left(\frac{\delta p_{\parallel s\mathbf{k}_\perp}}{2} + \delta p_{\perp s\mathbf{k}_\perp} \right) \left(\frac{-ik_y \phi_{\mathbf{k}_\perp}}{B} \right)^* \right] \right\rangle, \tag{5}$$

$$Q_{em,s} = \sum_{\mathbf{k}_\perp} \left\langle Re \left[\left(\frac{\delta q_{\parallel s\mathbf{k}_\perp}}{2} + \delta q_{\perp s\mathbf{k}_\perp} \right) \left(\frac{ik_y A_{\parallel \mathbf{k}_\perp}}{B} \right)^* \right] \right\rangle, \tag{6}$$

$$\delta p_{\parallel s\mathbf{k}_\perp} = \int m_s v_\parallel^2 \delta f_{s\mathbf{k}_\perp} J_{0s} d^3 v, \qquad \delta p_{\perp s\mathbf{k}_\perp} = \int \mu B \delta f_{s\mathbf{k}_\perp} J_{0s} d^3 v, \tag{7}$$

$$\delta q_{\parallel s\mathbf{k}_\perp} = \int m_s v_\parallel^3 \delta f_{s\mathbf{k}_\perp} J_{0s} d^3 v - 3 T_s \delta u_{s\mathbf{k}_\perp}, \tag{8}$$

$$\delta q_{\perp s\mathbf{k}_\perp} = \int \mu B v_\parallel \delta f_{s\mathbf{k}_\perp} J_{0s} d^3 v - T_s \delta u_{s\mathbf{k}_\perp}, \tag{9}$$

and

$$\delta u_{s\mathbf{k}_\perp} = \int v_\parallel \delta f_{s\mathbf{k}_\perp} J_{0s} d^3 v. \tag{10}$$

Comparison of the MFC scan (red curve) with the MFF using the equilibrium at $\beta = 0$ (blue curve) implies that the influence of the Shafranov shift enhances the turbulent energy transport by the MFC, and the energy transport coefficients χ_i and χ_e for the MFC do not decrease with increasing β. This implies that there is no electromagnetic stabilizing effect on the turbulent transport, consistent with the results from the $s - \alpha$ model [26].

The significant difference from the $s - \alpha$ model is the increase of χ_i for both the MFC and MFF in Fig. 9. In the $s - \alpha$ model, χ_i is almost constant for the MFC scan, while χ_i decreases for the MFF [26]. A similar increase of χ_e is observed for the MFC and MFF in Fig. 9, whereas χ_e remains almost unchanged for the MFF in the $s - \alpha$ model. It is noted that the contribution of magnetic fluctuations to the energy transport is small. We encounter the runaway/non-zonal transition, which is the growth of fluctuations without saturation [41–43], at $\beta > 1.2\%$, so that χ_i and χ_e are not evaluated at $\beta > 1.2\%$. The turbulent transport at higher β can be evaluated by global gyrokinetic simulations which have an additional saturation mechanism such as the turbulence spreading [44].

We have observed the increase of χ_i with β for the MFF, although the MFF exhibits the decrease of linear growth rate of the ITG mode with β in Fig. 6. Here, we discuss this increase of χ_i with β for the MFF in detail. The increase of χ_i is due to intermittent bursts of turbulent fluctuations. Figure 10 (a) shows the time evolution of the ion energy diffusivity χ_i. The diffusivity χ_i for $\beta = 1.2\%$ intermittently increases to much larger value than its initial saturation level at $t \simeq 30$ and 95 $[R_0/v_{Ti}]$. On the other hand, the fluctuations of χ_i for $\beta = 0.4\%$ and 0.8% do not exhibit such intermittent bursts. Figure 10 (b) shows the time evolution of χ_i evaluated from the $s - \alpha$ model for the MFF (without Shafranov shift) [26]. The fluctuations of χ_i do not exhibit intermittent bursts even at $\beta = 1.2\%$, and χ_i decreases with increasing β. Thus, the intermittent bursts are the cause of the higher χ_i at higher β for the MFF scan from the numerically calculated MHD equilibrium in Fig. 9. These intermittent bursts at higher β consist of low-wavenumber fluctuations at $k_y\rho_{Ti} \leq 0.2$ as shown in Fig. 11. Figure 11 (a) shows the poloidal wavenumber spectrum of the ion energy diffusivity for the MFF. The diffusivity χ_i peaks around $k_y\rho_{Ti} = 0.2$ and increases as β increases, resulting in the higher χ_i at higher β in Fig. 9. On the other hand, when we average χ_i over $40 \leq t \leq 80$ to exclude the intermittent bursts for $\beta = 1.2\%$, χ_i is significantly reduced at low wavenumber $k_y\rho_{Ti} \leq 0.2$ in Fig. 11 (b). This indicates that the intermittent bursts are caused by low-wavenumber $k_y\rho_{Ti} \leq 0.2$ fluctuations, and these larger-scale fluctuations significantly enhance χ_i at higher β. As a result, when we exclude the intermittent bursts at $\beta_i = 1.2\%$, χ_i decreases with increasing β in Fig. 12 as expected from the linear growth rate for the MFF scan. Thus, the higher χ_i at higher β in Fig. 9 is due to the intermittent bursts with long-wavelength fluctuations at higher β. In addition, it is found that zonal flows become significantly weak when the bursts appear as shown in Fig. 13, and thus the temporal weakening of zonal flows can be the cause of the bursts. We will investigate the details of these bursts in our future work.

V. SUMMARY

We have investigated the β dependence of turbulent transport in self-consistent numerical MHD equilibrium states of a tokamak plasma at finite β by gyrokinetic simulations. The MHD equilibrium state is calculated for each value of β using the VMEC code and is consistent with the Cyclone base case DIII-D parameters. We have compared two β scans:

a scan with background magnetic field structure change (MFC) as β increases and a scan with remaining magnetic field structure fixed (MFF). The MFC includes the influence of the background magnetic field change with β such as the Shafranov shift due to the Pfirsch-Schluter current, while the MFF includes only the increase of the amplitude of magnetic fluctuations due to the increase of β.

The linear growth rate of drift-wave instabilities and associated turbulent transport at finite β value are calculated using the GKV code. For the MFF scan, the electromagnetic stabilization due to magnetic fluctuations on the ITG mode is observed. The electromagnetic stabilization is obtained for three MFF scans using the MHD equilibrium at $\beta = 0$, 1.2% and 2.4% calculated by the VMEC code. For the MFC scan, by contrast, the stabilization is canceled out by the influence of the Shafranov shift, and thus the growth rate of the ITG mode remains unchanged as β increases, consistent with the calculation using the $s - \alpha$ model [26], while the enhancement of the growth rate is larger than that from the $s - \alpha$ model. This influence of the Shafranov shift can be understood by examining the dispersion relation of electromagnetic ITG modes (Eq. (1)). The dispersion relation implies that the reduction of $k_\perp^2$ by the MFC enhances the electromagnetic stabilization, while the reduction of ω_d by the MFC reduces the stabilization. Then, the influence of the MFC on ω_d is found to be larger than that on $k_\perp^2$ by our simulations, leading to the enhancement of the growth rate of the ITG mode. The dispersion relation also implies that the electromagnetic stabilizing effect on the ITG mode is enhanced by small $k_\parallel$, which can be realized in weak magnetic shear plasmas.

The significant difference of the MFC scan from the $s - \alpha$ model is that the critical onset β value for the KBM is significantly increased from $\beta = 2.6\%$ to $\beta > 4.8\%$. This is because the validity of the $s - \alpha$ model is gradually diminished with increasing β compared to the self-consistent MHD equilibrium calculated by the VMEC code.

The energy transport coefficients χ_i and χ_e are evaluated by nonlinear simulations. The ion energy transport increases with β for both the MFC and MFF scans, while the increasing rate is larger for the MFC. The electron energy transport also increases with β for both the MFC and MFF scans, while the transport rapidly increases for the MFC. The larger transport in the MFC scan than the MFF is consistent with the results from the $s - \alpha$ model [26]. On the other hand, the higher χ_i at higher β in the MFF scan without Shafranov shift is in contrast to the results from the $s - \alpha$ model. The MFF scan from the $s - \alpha$ model

exhibits the lower χ_i at higher β. The increase of χ_i with β in the MFF scan from the numerically calculated equilibrium is due to the intermittent bursts with long-wavelength fluctuations at higher β, which are related to a temporal reduction of zonal flows.

APPENDIX A: COMPARISON BETWEEN $s - \alpha$ MODEL AND NUMERICAL MHD EQUILIBRIUM WITH LARGE ASPECT RATIO

Here, we discuss the deviation of the $s - \alpha$ model from the corresponding numerical MHD equilibrium. The deviation is due to the inconsistency of the $s - \alpha$ model as shown below. Since a large aspect ratio approximation is used in deriving the $s - \alpha$ model, we can make $k_\perp^2$ and ω_d be close to those of $s - \alpha$ model by setting a large aspect ratio as shown in Fig. 14. Figure 14 shows the profiles of the strength of the magnetic field B, the square of perpendicular wavenumber $k_\perp^2$ and the ion magnetic drift frequency ω_{di} along a field line coordinate z for the CBC from the $s - \alpha$ model with $a/R_0 = 0.36$, for the CBC calculated by the VMEC with $a/R_0 = 0.36$, and for the CBC with a large aspect ratio $a/R_0 = 0.04$ by the VMEC. The β value is set to be zero in this analysis.

The perpendicular wavenumber $k_\perp^2$ of the VMEC equilibrium with the large aspect ratio $a/R_0 = 0.04$ is very close to that of the $s - \alpha$ model with $a/R_0 = 0.36$ as shown in Fig. 14 (b), and is enhanced by decreasing the inverse aspect ratio from $a/R_0 = 0.36$ to $a/R_0 = 0.04$. The magnetic drift frequency ω_{di} of the VMEC equilibrium with $a/R_0 = 0.04$ is also very close to that of the s-α model with $a/R_0 = 0.36$ as shown in Fig. 14 (c). On the other hand, the profile of the strength of magnetic field B of the VMEC equilibrium with $a/R_0 = 0.04$ is significantly different from that of the s-α model with $a/R_0 = 0.36$ as shown in Fig. 14 (a), and thus the mirror-ratio of the VMEC equilibrium with the large aspect ratio $a/R_0 = 0.04$ is much smaller than that with $a/R_0 = 0.36$. We will show that this small mirror-ratio has strong impact on the stability of the ITG mode. Figure 15 shows the linear growth rate of drift-wave instabilities calculated for these three equilibrium states. The ITG mode is unstable at low wavenumber, while the TEM is unstable at high wavenumber. The VMEC equilibrium with $a/R_0 = 0.36$ is more unstable against the ITG mode than the $s - \alpha$ model. On the other hand, the growth rate of the ITG mode for the VMEC equilibrium with the large aspect ratio $a/R_0 = 0.04$ is much lower than that from the $s - \alpha$ model, even though $k_\perp^2$ and ω_{di} are very similar to those of the $s - \alpha$ model. This small growth rate for the VMEC

equilibrium with the large aspect ratio $a/R_0 = 0.04$ is due to its small mirror-ratio, because the fraction of trapped electrons has significant impact on the growth rate of ITG modes. Thus, the differences between the $s - \alpha$ model and the numerical equilibrium calculated by the VMEC code shown in Fig. 4 is mainly caused by the inconsistent large-aspect-ratio approximation used in the $s - \alpha$ model.

Finally, in order to understand the aspect ratio dependence of the Shafranov shift effect, we have carried out an additional β scan for a small-aspect-ratio plasma with $\epsilon = 0.38$ at $\rho = 0.5$, i.e. $a/R_0 = 0.76$. Figure 16 shows the linear growth rate as a function of β, and presents a similar enhancement of the growth rate by the influence of the Shafranov shift as those with $\epsilon = 0.18$ in Sec. 3, and thus our conclusions are valid even in small-aspect-ratio toroidal plasmas.

DATA AVAILABILITY STATEMENT

The data that support the findings of this study are available upon reasonable request from the authors.

[1] W. Horton, Rev. Mod. Phys. **71**, 735, (1999).

[2] W. Horton, *Turbulent Transport in Magnetized Plasmas*, World Scientific (2012).

[3] H. Urano, T. Takizuka, H. Takenaga, N. Oyama, Y. Miura, and Y. Kamada, Nucl. Fusion **46**, 781 (2006).

[4] L. Vermare, F. Ryter, C. Angioni, A. G. Peeters, J. Stober, R. Bilato, L. D. Horton, B. Kurzan, C. F. Maggi, H. Meister, J. Schirmer, G. Tardini (The ASDEX Upgrade Team), Nucl. Fusion **47**, 490 (2007).

[5] C. C. Petty, Phys. Plasmas **15**, 080501 (2008).

[6] D. C. McDonald, L. Laborde, J. C. Deboo, F. Ryter, M. Brix, C. D. Challis, P. de Vries, C. Giroud, D. Howell, E. Joffrin, T. C. Luce, J. Mailloux, V. Pericoli-Ridolfini, A. C. C. Sips, K. Thomsen and JET EFDA Contributors, Plasma Phys. Controlled Fusion **50**, 124013 (2008).

[7] C. D. Challis et al., Nucl. Fusion **55**, 053031 (2015).

[8] W. M. Tang, J. W. Connor, R. J. Hastie, Nucl. Fusion **20**, 1439 (1980).

[9] A. Hirose, Phys. Plasmas **7**, 433 (2000).

[10] K. Aleynikova and A. Zocco, Phys. Plasmas **24**, 092106 (2017).

[11] T. S. Hahm, W. W. Lee, and A. Brizard, Physics of Fluids **31**, 1940 (1988).

[12] J.Y. Kim, W. Horton and J.Q. Dong, Phys. Fluids **B 5** 4030 (1993).

[13] J. Candy, Phys. Plasmas **12**, 072307 (2005).

[14] M. J. Pueschel, M. Kammerer, and F. Jenko, Phys. Plasmas **15**, 102310 (2008).

[15] M. J. Pueschel and F. Jenko, Phys. Plasmas **17**, 062307 (2010).

[16] A. Ishizawa, S. Maeyama, T.-H.Watanabe, H. Sugama and N. Nakajima, Journal of Plasma Physics **81**, 435810203 (2015).

[17] G. G. Whelan, M. J. Pueschel, P. W. Terry, Phys. Rev. Lett. **120** 175002 (2018).

[18] J. Citrin, F. Jenko, P. Mantica, D. Told, C. Bourdelle, J. Garcia, J.W. Haverkort, G. M. D. Hogeweij, T. Johnson, and M. J. Pueschel, Phys. Rev. Lett. **111** 155001 (2013).

[19] J. Citrin, J. Garcia, T. Grler, F. Jenko, P. Mantica, D. Told, C. Bourdelle, D. R. Hatch, G. M. D. Hogeweij, T. Johnson, M. J. Pueschel, M. Schneider and JET-EFDA Contributors, Plasma Phys. Control Fusion **57**, 014032 (2015).

[20] H. Doerk, M. Dunne, F. Jenko, et al., Phys. Plasmas **22**, 042503 (2015).

[21] J. Garcia, et.al., Nucl. Fusion **55**, 053007 (2015).

[22] H. Doerk, et.al., Plasma Phys. Control. Fusion **58**, 115005 (2016).

[23] J. Garcia and JET Contributors, Plasma Phys. Control. Fusion **64**, 104002 (2022).

[24] A. Ishizawa, T.-H. Watanabe, H. Sugama, M. Nunami, K. Tanaka, S. Maeyama and N. Nakajima, Nuclear Fusion **55**, 043024 (2015).

[25] I.J. McKinney, M.J. Pueschel, B.J. Faber, C.C. Hegna, A. Ishizawa, P.W. Terry, Journal of Plasma Physics **87**, 905870311 (2021).

[26] A. Ishizawa, D. Urano, Y. Nakamura, S. Maeyama, and T.-H. Watanabe, Phys. Rev. Lett. **123**, 025003 (2019).

[27] D. R. Hatch, M. J. Pueschel, F. Jenko, W. M. Nevins, P.W. Terry, and H. Doerk, Phys. Rev. Lett. **108** 235002 (2012).

[28] P. W. Terry, M. J. Pueschel, D. Carmody, and W. M. Nevins, Phys. Plasmas **20**, 112502 (2013).

[29] Z. R. Williams, M. J. Pueschel, P. W. Terry, and T. Hauff, Phys. Plasmas **24**, 122309 (2017).

[30] P. Mantica, D. Strintzi, T. Tala, et.al., Phys. Rev. Lett. **102**, 175002 (2009).

[31] P. Mantica, C. Angioni, C. Challis, et.al., Phys. Rev. Lett. **107**, 135004 (2011).

[32] J.W. Connor, R. J. Hastie, and J. B. Taylor, Phys. Rev. Lett. **40**, 396 (1978).

[33] A. Hirose, L. Zhang, and M. Elia, Phys. Rev. Lett. **72** 3993 (1994).

[34] X. Lapillonne, S. Brunner, T. Dannert, S. Jolliet, A. Marinoni, L. Villard, T. Gorler, F. Jenko, and F. Merz, Physics of Plasmas **16**, 032308 (2009).

[35] Gary M. Staebler, Nuclear Fusion **58**, 115001 (2018).

[36] T.-H. Watanabe and H. Sugama, Nucl. Fusion **46** 24 (2006).

[37] A. Ishizawa, S. Maeyama, T.-H.Watanabe, H. Sugama, and N. Nakajima, Nucl. Fusion **53**, 053007 (2013).

[38] M. Nunami, T.-H. Watanabe, H. Sugama, Plasma and Fusion Research **5**, 016 (2010).

[39] S. P. Hirshman and J. C. Whitson, Phys. Fluids **26**, 3553 (1983).

[40] N. Joiner, A. Hirose, and W. Dorland, Phys. Plasmas **17**, 072104 (2010).

[41] R. E. Waltz, Phys. Plasmas **17**, 072501 (2010).

[42] M. J. Pueschel, P.W. Terry, F. Jenko, D. R. Hatch, W. M. Nevins, T. Gorler, and D. Told, Phys. Rev. Lett. **110**, 155005 (2013).

[43] M. J. Pueschel, P. W. Terry, and D. R. Hatch, Phys. Plasmas **21**, 055901 (2014).

[44] H. Masui, A. Ishizawa, K. Imadera, Y. Kishimoto, Y. Nakamura, Nuclear Fusion 62, 074001 (2022).
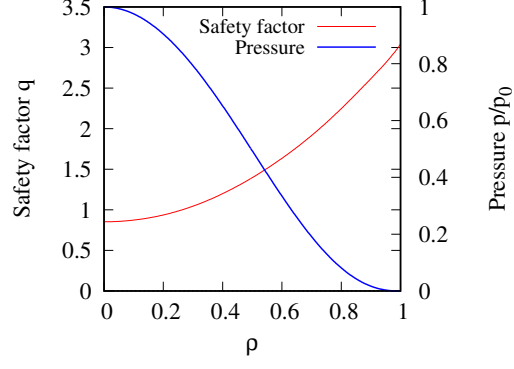
FIG. 1: The pressure p and safety factor q profiles.
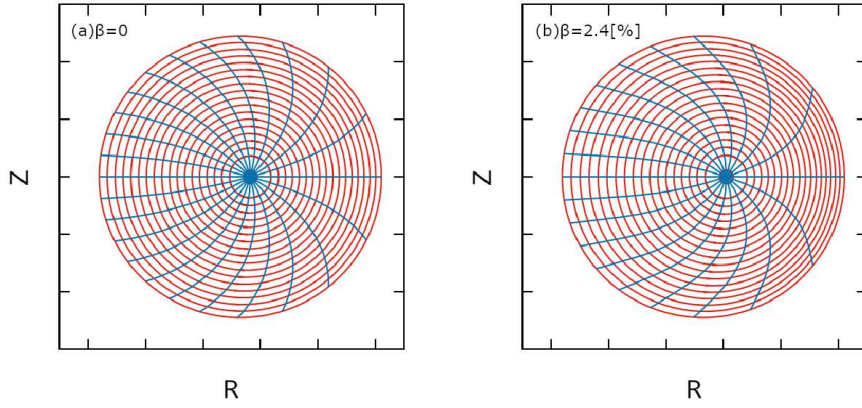
FIG. 2: Magnetic surfaces (red curve) and constant poloidal angle lines (blue curve) on a cross section at (a) $\beta = 0$ and (b) 2.4%.
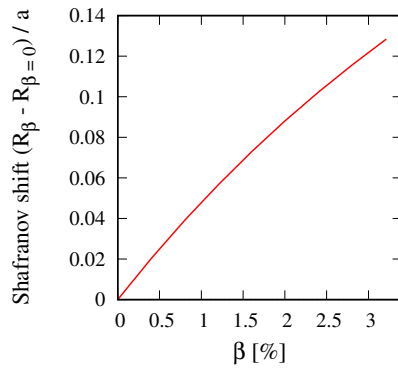
FIG. 3: The Shafranov shift normalized by the minor radius $(R(\beta) - R(\beta = 0))/a$ as a function of β.
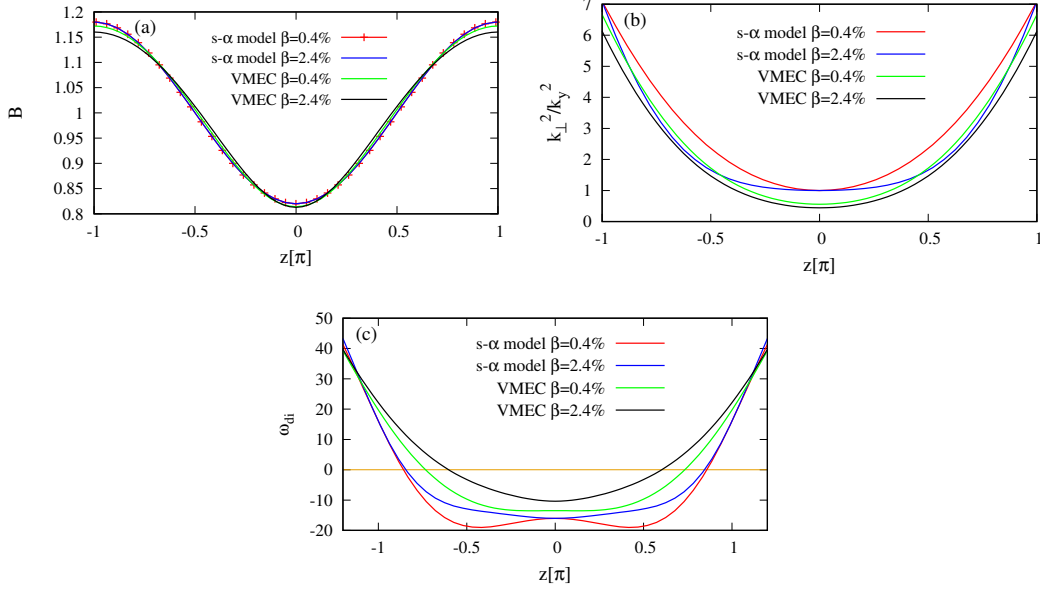
FIG. 4: (a) Magnetic field strength B, (b) square of perpendicular wavenumber $k_\perp^2$, and (c) ion magnetic drift frequency ω_{di} as a function of the coordinate along the field line z from the $s-\alpha$ model and numerical equilibrium states from the VMEC code at $\beta = 0.4\%$ and 2.4%.
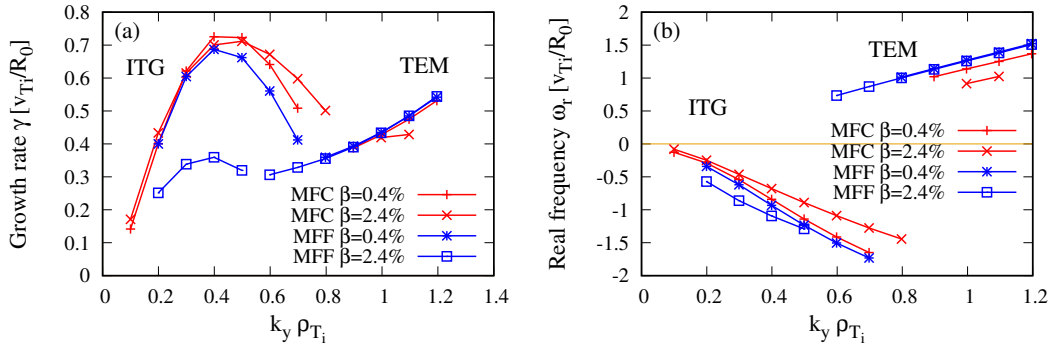
FIG. 5: (a) Linear growth rate γ and (b) real frequency ω of drift-wave instabilities as a function of wavenumber k_y at $\beta = 0.4\%$ and 2.4% for the magnetic field change (MFC: with the Shafranov shift) scan and the magnetic field fixed (MFF: without the Shafranov shift) scan.
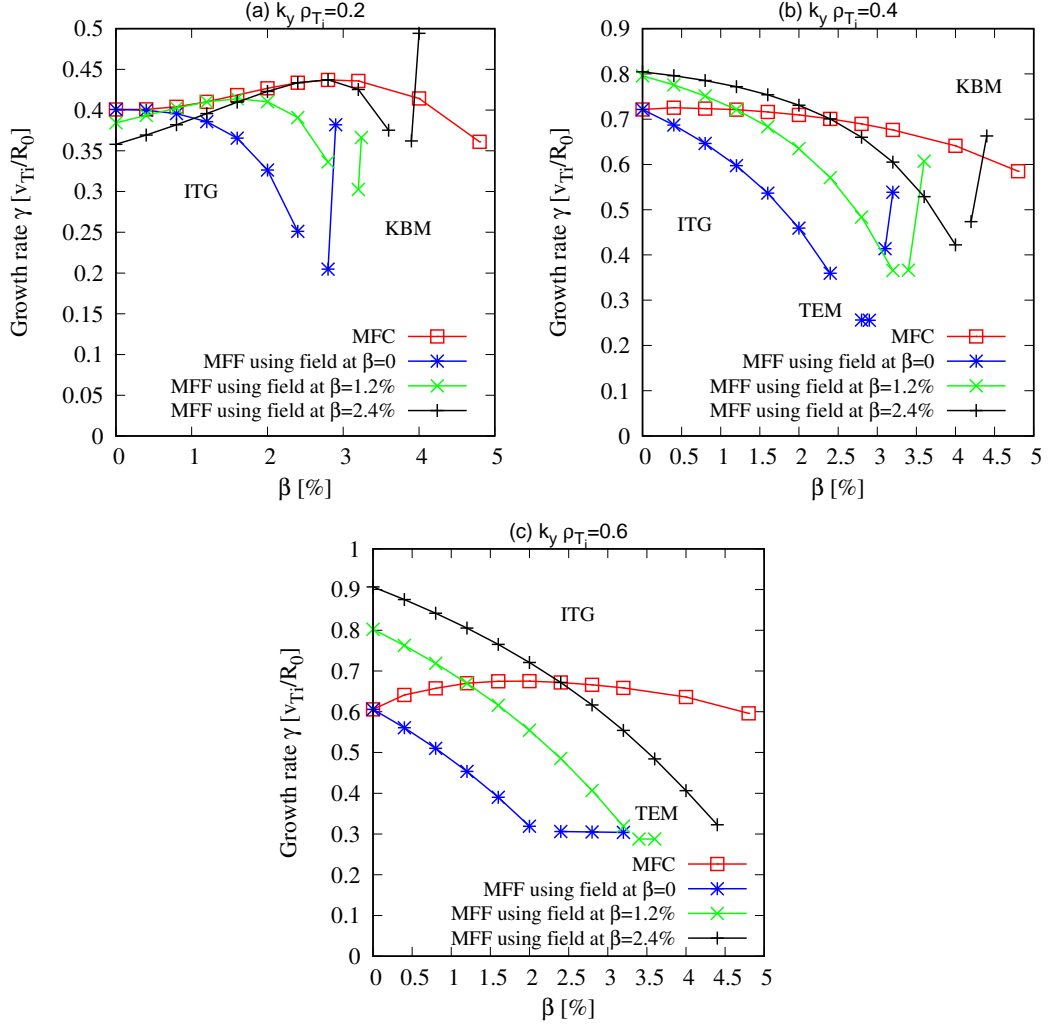
FIG. 6: Linear growth rate γ of drift-wave instabilities as a function of β at (a) $k_y\rho_{Ti} = 0.2$, (b) 0.4, and (c) 0.6 for the MFC (with the Shafranov shift: red curve), MFF using equilibrium at $\beta = 0\%$ (without the Shafranov shift: blue curve), MFF using equilibrium at $\beta = 1.2\%$ (fixed Shafranov shift: green curve), and MFF using equilibrium at $\beta = 2.4\%$ (fixed Shafranov shift: black curve).
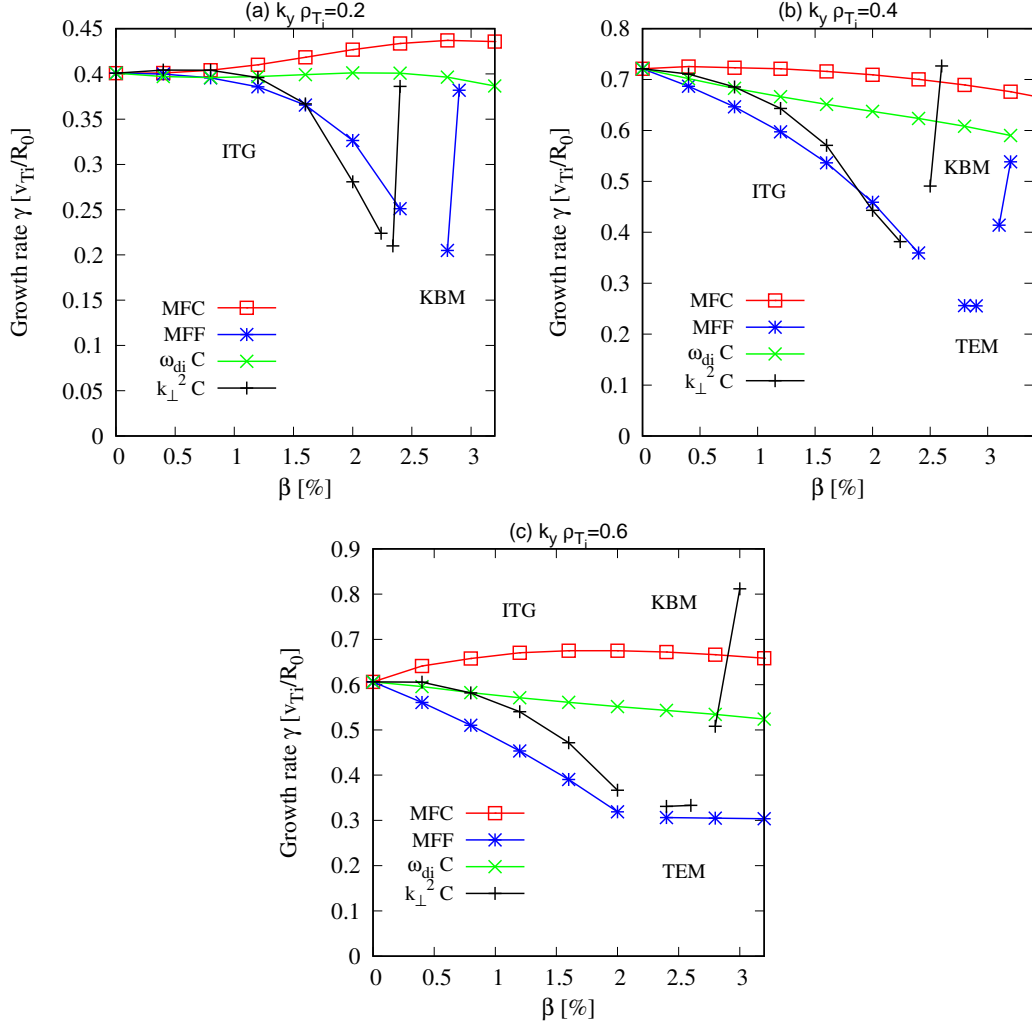
FIG. 7: Linear growth rate γ of drift-wave instabilities as a function of β at (a) $k_y\rho_{Ti} = 0.2$, (b) 0.4, and (c) 0.6 for the MFC (with the Shafranov shift: red curve) and MFF (without the Shafranov shift: blue curve). The magnetic field changed only in ω_{di} ($\omega_{di}C$) and only in $k_\perp^2$ ($k_\perp^2 C$) cases are added.
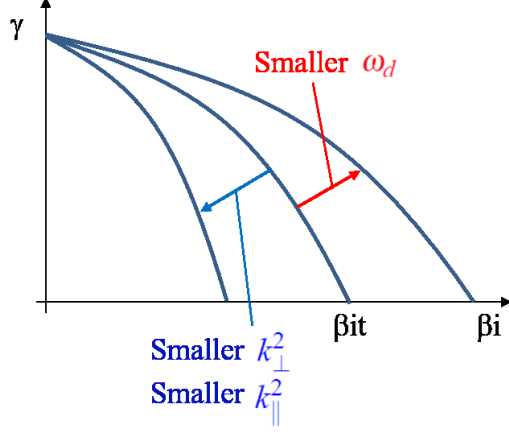
FIG. 8: Schematic of the influence of $k_\perp^2$, ω_{di} and $k_\parallel^2$ on the β dependence of the growth rate of the ITG mode, where $\beta_i = \beta/(1 + T_e/T_i)$.
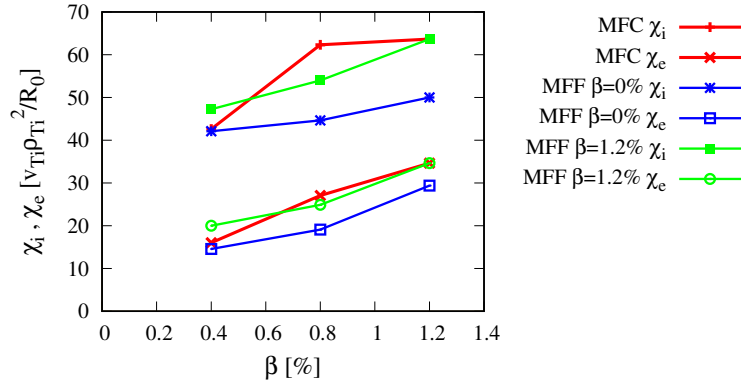
FIG. 9: Ion and electron energy diffusivity χ_i and χ_e as a function of β for the MFC (with the Shafranov shift), MFF (without the Shafranov shift) using equilibrium at $\beta = 0$, and MFF using equilibrium at $\beta = 1.2\%$ (fixed Shafranov shift).
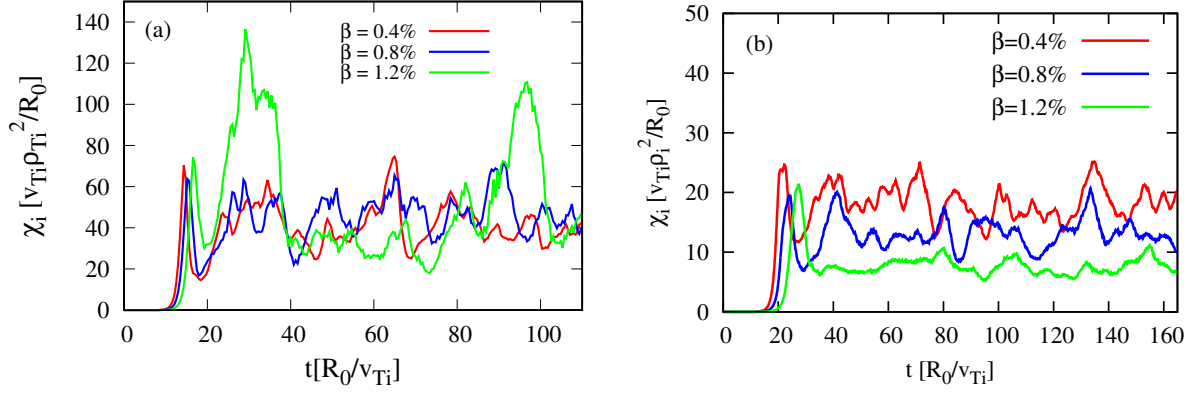
FIG. 10: Time evolution of ion energy diffusivity χ_i for the MFF (without Shafranov shift) at $\beta = 0.4\%$, 0.8% and 1.2% (a) from the numerically calculated MHD equilibrium state and (b) from the $s - \alpha$ model.
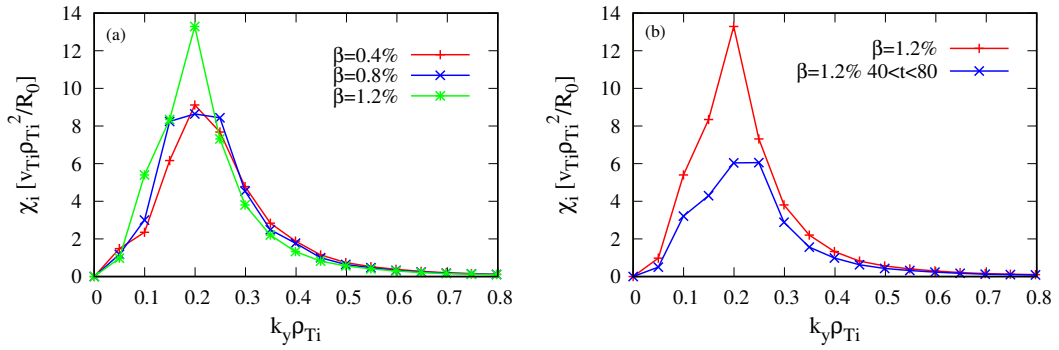
FIG. 11: (a) Spectrum of ion energy diffusivity χ_i for the MFF (without the Shafranov shift) and (b) spectrum of χ_i for the MFF at $\beta = 1.2\%$ including intermittent bursts and excluding the bursts by averaging over $40 \leq t \leq 80$.
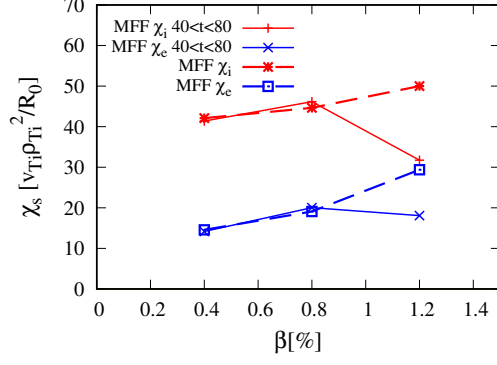
FIG. 12: Ion and electron energy diffusivity χ_i and χ_e as a function of β for the MFF (without the Shafranov shift) including intermittent bursts and excluding intermittent bursts by averaging over $40 \leq t \leq 80$.
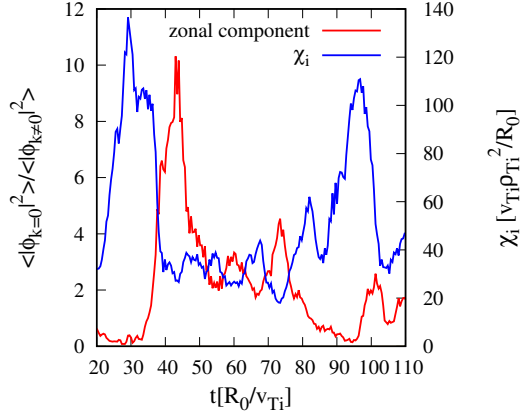

FIG. 13: Time evolution of ion energy diffusivity χ_i and the ratio of the zonal component to turbulent component of the electrostatic potential $\langle |\phi(k_y = 0)|^2 \rangle / \sum_{k_y \neq 0} \langle |\phi(k_y)|^2 \rangle$ for the MFF (whiteout the Shafranov shift) at $\beta = 1.2\%$.
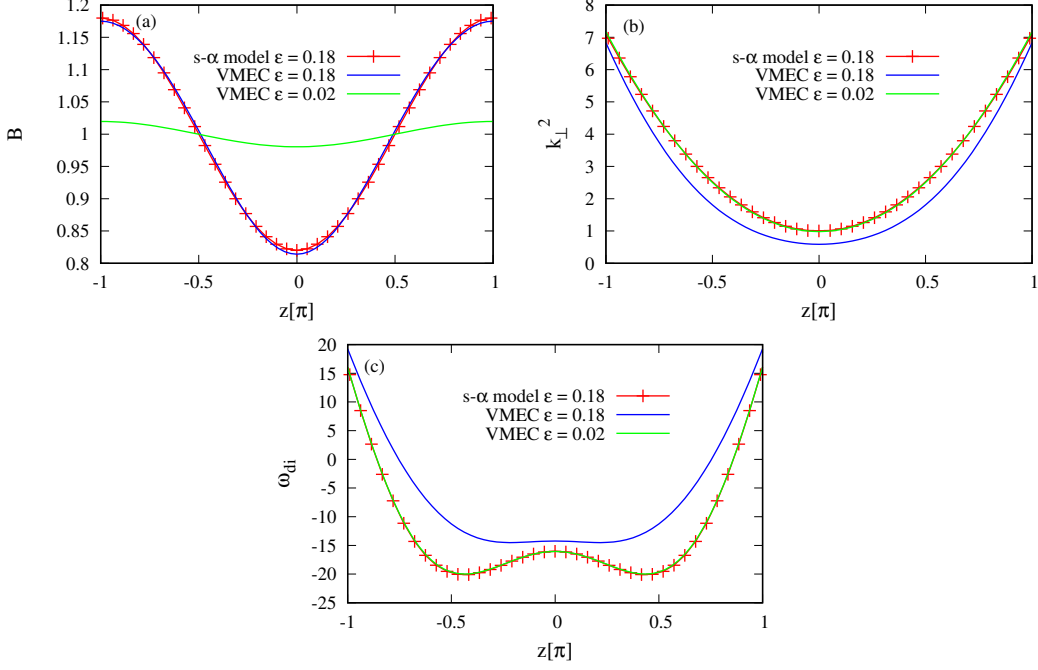
FIG. 14: (a) Magnetic field strength B, (b) square of perpendicular wavenumber $k_\perp^2$, and (c) ion magnetic drift frequency ω_{di} for the $s-\alpha$ model with $\epsilon = (a/2)/R_0 = 0.18$, for the equilibrium calculated by VMEC with $\epsilon = (a/2)/R_0 = 0.18$, and for the equilibrium by VMEC with a large aspect ratio $\epsilon = (a/2)/R_0 = 0.02$.
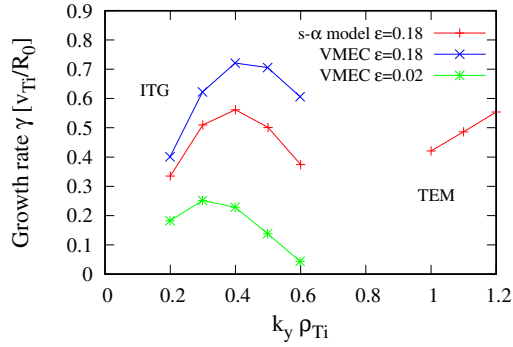

FIG. 15: Linear growth rate γ as a function of the poloidal wavenumber k_y for the $s-\alpha$ model with $\epsilon = (a/2)/R_0 = 0.18$, for the equilibrium calculated by VMEC with $\epsilon = (a/2)/R_0 = 0.18$, and for the equilibrium by VMEC with a large aspect ratio $\epsilon = (a/2)/R_0 = 0.02$.
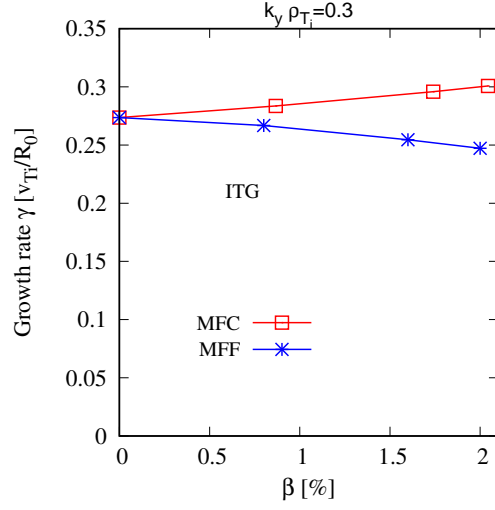
FIG. 16: Linear growth rate γ of the ITG mode at $\rho = 0.5$ in a small-aspect-ratio tokamak with $a/R_0 = 0.76$ as a function of β at $k_y\rho_{Ti} = 0.3$ for the MFC (with the Shafranov shift: red curve) and MFF (without the Shafranov shift: blue curve).